The Taylor-Culick profile with arbitrary headwall injection

Joseph Majdalani[a)] and Tony Saad
University of Tennessee Space Institute, Tullahoma, Tennessee 37388, USA

(Received 4 June 2006; accepted 23 March 2007; published online 5 September 2007)

Taylor's incompressible and rotational profile is extended to a porous cylinder with arbitrary headwall injection. This profile, often referred to as Culick's mean flow, is now generalized to permit the imposition of reactive headwall conditions. Starting with Euler's steady equations, the solution that we derive is approximate, being exact only at the sidewall, the centerline, or for similarity-conforming inlet profiles. Furthermore, the approximation is quasiviscous, being observant of the no slip requirement at the sidewall. Based on numerical experiments under inviscid flow conditions, the closed-form approximation that we obtain appears to be well suited to describe the bulk flow field in basic models of solid and hybrid rockets where uniform sidewall injection is imposed at the propellant surface. For similarity-nonconforming profiles, the approximation becomes more accurate as we move away from the headwall. Results are verified using computational fluid dynamics for several headwall injection patterns. *© 2007 American Institute of Physics*. [DOI: 10.1063/1.2746003]

I. INTRODUCTION

Culick's solution for describing the gaseous motion in solid rocket motors (SRMs) was obtained under the contingencies of steady, incompressible, rotational, axisymmetric, and quasiviscous flow.[1] Despite being strictly inviscid, its streamlines observed the no slip requirement along the porous wall. It also coincided with Taylor's expression obtained a decade earlier, albeit in an entirely different physical context.[2] As noted by many specialists in the propulsion field, the corresponding mean flow was driven by inviscid pressure forces and did not need viscosity to exhibit vorticity or satisfy the apparent no-slip condition at the porous sidewall. Furthermore, the often cited Taylor-Culick profile was repeatedly verified in a number of investigations. These start with the inventive tests reported by Taylor[2] and continue to those carried out in later years by way of computation (Dunlap, Willoughby, and Hermsen;[3] Baum, Levine, and Lovine;[4] Sabnis, Gibeling, and McDonald[5]), laboratory experiments (Yamada, Goto, and Ishikawa;[6] Dunlap *et al.*[7]), and theory (Clayton;[8] Balachandar, Buckmaster, and Short;[9] Majdalani and Roh;[10] Majdalani and Flandro[11]). In short, a collective body of research has confirmed the suitability of the Taylor-Culick model in approximating the bulk flow in a full-length cylindrical motor (Kuentzmann;[12] Traineau, Hervat, and Kuentzmann;[13] Apte and Yang[14]). Due to its robustness, this profile has stood at the foundation of many theoretical studies, especially, those concerned with wave propagation (Majdalani and Flandro[11]) and both hydrodynamic and combustion instability theories in porous chambers including those that account for particle interactions (Griffond and Casalis;[15,16] Féraille and Casalis[17]).

The Taylor-Culick profile has also been extended to simulate solid rocket motors with regressing walls. This was accomplished using a nozzleless, nonreactive, rotational, viscous, and incompressible approximation that employs similarity in time to model the expansion pattern of the porous wall.[18] It has also been submitted by Majdalani and Vyas[19] as a basic model for simulating the bulk motion in hybrid rockets exhibiting circular-port fuel grains. This was achieved by imposing a sinusoidal headwall injection profile to mimic oxidizer injection. In this article, we extend the solution by incorporating variable headwall injection in the context of steady, incompressible, axisymmetric, inviscid, and rotational flow. We first derive the solution for uniform headwall injection to the extent of making it applicable to solid and hybrid rockets in which the inflow at the headwall is nearly uniform. The headwall-to-sidewall injection velocity ratio will be considerably larger in the case of hybrids, thus leading to the onset of stream tube motion. The present solution, based on the vorticity stream function approach, will fully capture this behavior. The resulting formulation will provide an elemental approximation as it discounts the effects of compressibility, mixing, viscosity, and chemical reactions. However, by satisfying the no slip condition on the walls, the solution will exhibit a quasiviscous trait akin to that displayed by the Taylor-Culick profile. The same may be said of the solution that we then formulate for arbitrary headwall injection. The ensuing representation will permit the incorporation of practical injection scenarios that can be verified numerically.

II. MATHEMATICAL MODEL

As usual, a rocket motor can be idealized as a cylindrical chamber of porous length L_0 and radius a with both a reactive headwall and a nozzleless aft end (see Fig. 1). At the headwall, a fluid stream (which may denote an oxidizer or gaseous propellant mixture) is injected into the chamber at a prescribed velocity $\bar{u}_0$; this could be given by

[a)]Author to whom correspondence should be addressed. Department of Mechanical, Aerospace and Biomedical Engineering, University of Tennessee (UTSI), 411 B. H. Goethert Parkway, Tullahoma, Tennessee 37388-9700. Electronic mail: drmajdalani@gmail.com

1070-6631/2007/19(9)/093601/10/$23.00

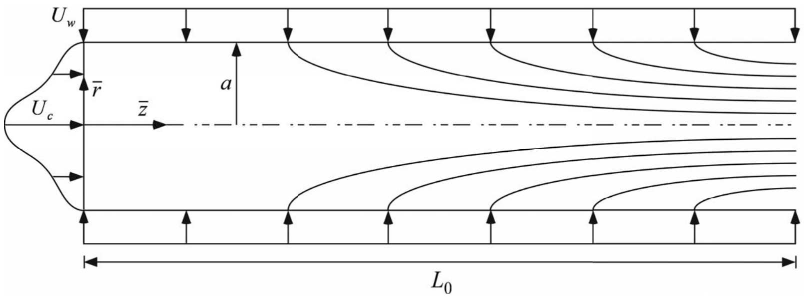

FIG. 1. Sketch of a porous tube with variable headwall injection.

$$\bar{u}_0(\bar{r}) = \begin{cases} U_c = \text{const}; & \text{uniform} \\ U_c \cos\left(\frac{1}{2}\pi\bar{r}^2/a^2\right); & \text{half-cosine} \\ U_c[1-(\bar{r}/a)^m]; & \text{laminar and turbulent} \\ U_c(1-\bar{r}/a)^{1/m}; & \text{turbulent} \end{cases} \tag{1}$$

where $U_c = \bar{u}_z(0,0)$ is the centerline velocity at the headwall (a constant), m is some integer, and the overbar denotes dimensional variables. The incoming stream merges with the crossflow sustained by uniform mass addition along the porous sidewall. Naturally, the sidewall injection velocity $U_w = -\bar{u}_r(a,\bar{z})$ is commensurate with propellant or fuel regression rates. In hybrids, U_w can be appreciably smaller than U_c due to slow fuel pyrolysis; in SRM analysis, these two values are identical. As shown in Fig. 1, $\bar{r}$ and $\bar{z}$ stand for the radial and axial coordinates used to describe the solution from the headwall to the typical nozzle attachment point at the aft end. The solution that we seek applies, in particular, to simulated rocket motors and, in general, to injection-driven porous tubes with headwall injection.

A. Normalization

For expediency, it is helpful to normalize all recurring variables and operators. This can be done by setting

$$r = \frac{\bar{r}}{a}; \quad z = \frac{\bar{z}}{a}; \quad \nabla = a\bar{\nabla}; \quad p = \frac{\bar{p}}{\rho U_w^2}; \quad \psi = \frac{\bar{\psi}}{a^2 U_w}; \tag{2}$$

$$u_r = \frac{\bar{u}_r}{U_w}; \quad u_z = \frac{\bar{u}_z}{U_w}; \quad \mathbf{\Omega} = \frac{\bar{\mathbf{\Omega}} a}{U_w}; \quad u_c = \frac{U_c}{U_w}; \quad L = \frac{L_0}{a}. \tag{3}$$

For steady inviscid motion, the vorticity transport equation reduces to

$$\nabla \times (\mathbf{u} \times \mathbf{\Omega}) = 0; \quad \mathbf{\Omega} = \nabla \times \mathbf{u}. \tag{4}$$

An assortment of four boundary conditions can be prescribed by writing

$$\begin{aligned} &u_r(0,z) = 0; && \text{no flow across centerline} \\ &u_z(1,z) = 0; && \text{no slip at sidewall} \\ &u_r(1,z) = -1; && \text{constant radial inflow at sidewall} \\ &u_z(r,0) = u_0(r); && \text{axial inflow at headwall} \end{aligned} \tag{5}$$

$$u_0(r) = \begin{cases} u_c = \text{const} \\ u_c \cos\left(\frac{1}{2}\pi r^2\right) \\ u_c(1-r^m) \\ u_c(1-r)^{1/m}. \end{cases}$$

B. Vorticity-stream function approach

Continuity is fulfilled by the Stokes stream function when it is written as

$$u_r = -\frac{1}{r}\frac{\partial \psi}{\partial z}; \quad u_z = \frac{1}{r}\frac{\partial \psi}{\partial r}. \tag{6}$$

Substitution into Eq. (4) requires

$$\Omega = rF(\psi), \tag{7}$$

so we follow tradition[1] and set

$$\Omega = C^2 r\psi. \tag{8}$$

Despite the nonuniqueness of this relation, it enables us to satisfy Eq. (4). Straightforward substitution into the vorticity equation yields the standard PDE,

$$\frac{\partial^2 \psi}{\partial z^2} + \frac{\partial^2 \psi}{\partial r^2} - \frac{1}{r}\frac{\partial \psi}{\partial r} + C^2 r^2 \psi = 0 \tag{9}$$

with the particular set of constraints,

$$\lim_{r\to 0}\frac{1}{r}\frac{\partial \psi(r,z)}{\partial z} = 0 \text{ (a)}; \quad \frac{\partial \psi(1,z)}{\partial r} = 0 \text{ (b)};$$
$$\frac{1}{r}\frac{\partial \psi(1,z)}{\partial z} = 1 \text{ (c)}; \quad \frac{1}{r}\frac{\partial \psi(r,0)}{\partial r} = u_0(r) \text{ (d)}. \tag{10}$$

By virtue of L'Hôpital's rule, removing the singularity in Eq. (10)(a) requires that both

$$\frac{\partial \psi(0,z)}{\partial z} = 0 \text{ (a)} \quad \text{and} \quad \frac{\partial^2 \psi(0,z)}{\partial r\,\partial z} = 0 \text{ (b)}. \tag{11}$$

Being linear, Eq. (9) is solvable by separation of variables; it yields

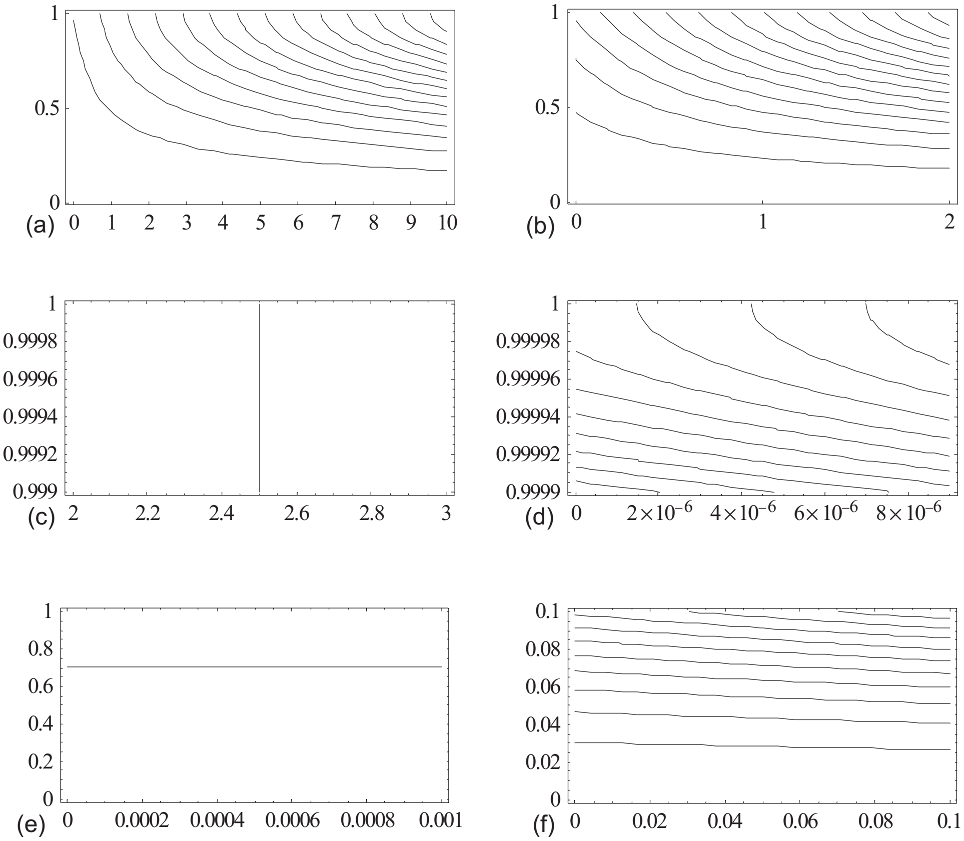

FIG. 2. Streamlines for $u_c=1$ depicted in the $r-z$ plane for the uniform headwall injection case. Results shown in (a)–(f) are enhancements that illustrate the streamline curvature in different sectors of the chamber.

$$\psi(r,z) = (\alpha z + \beta)\left[A \cos\left(\tfrac{1}{2}Cr^2\right) + B \sin\left(\tfrac{1}{2}Cr^2\right)\right]. \tag{12}$$

This expression satisfies Eq. (11)(b) identically. Thus, from this point forward, Eq. (10)(a) may be superseded by Eq. (11)(a).

III. SOLUTIONS

A. Solution by general eigenfunction expansions

Application of the boundary conditions must be carried out, preferably, in the order in which they appear. For example, Eq. (11)(a) gives

$$\frac{\partial \psi(0,z)}{\partial z} = \alpha A \cos\left(\tfrac{1}{2}Cr^2\right) + \alpha B \sin\left(\tfrac{1}{2}Cr^2\right)\Big|_{r=0} = 0 \tag{13}$$

or $A=0$. Without loss in generality, we set $B=1$ and rewrite Eq. (10)(b) as

$$rC(\alpha z + \beta)\cos\left(\tfrac{1}{2}Cr^2\right)\Big|_{r=1} = 0; \quad \forall z \tag{14}$$

and so $\cos(C/2)=0$; this is satisfied by

$$C = C_n = (2n+1)\pi; \quad n = \{0,1,2,\ldots,\infty\} \in \mathbb{N}. \tag{15}$$

Using $C_n=(2n+1)\pi$ enables us to sum over eigenfunctions corresponding to wall suction and injection. This process introduces an error term in Eq. (4) that will be examined later. We now put

$$\psi_n(r,z) = (\alpha_n z + \beta_n)\sin\left[\left(n+\tfrac{1}{2}\right)\pi r^2\right] \quad \text{or}$$
$$\psi(r,z) = \sum_{n=0}^{\infty} (\alpha_n z + \beta_n)\sin\left[\left(n+\tfrac{1}{2}\right)\pi r^2\right]. \tag{16}$$

The third condition becomes

$$\frac{\partial \psi(1,z)}{\partial z} = \sum_{n=0}^{\infty} \alpha_n \sin\left[\left(n+\tfrac{1}{2}\right)\pi\right] = 1 \quad \text{or}$$
$$\sum_{n=0}^{\infty} (-1)^n \alpha_n = 1. \tag{17}$$

This constraint may exhibit several outcomes depending on the behavior of α_n. Lastly, the headwall condition may be satisfied by evoking the ideas of superposition and orthogonality. Starting with

$$\frac{1}{r}\frac{\partial \psi(r,0)}{\partial r} = \pi \sum_{n=0}^{\infty} (2n+1)\beta_n \cos\left[\left(n+\tfrac{1}{2}\right)\pi r^2\right] = u_0(r) \tag{18}$$

one can apply orthogonality to secure

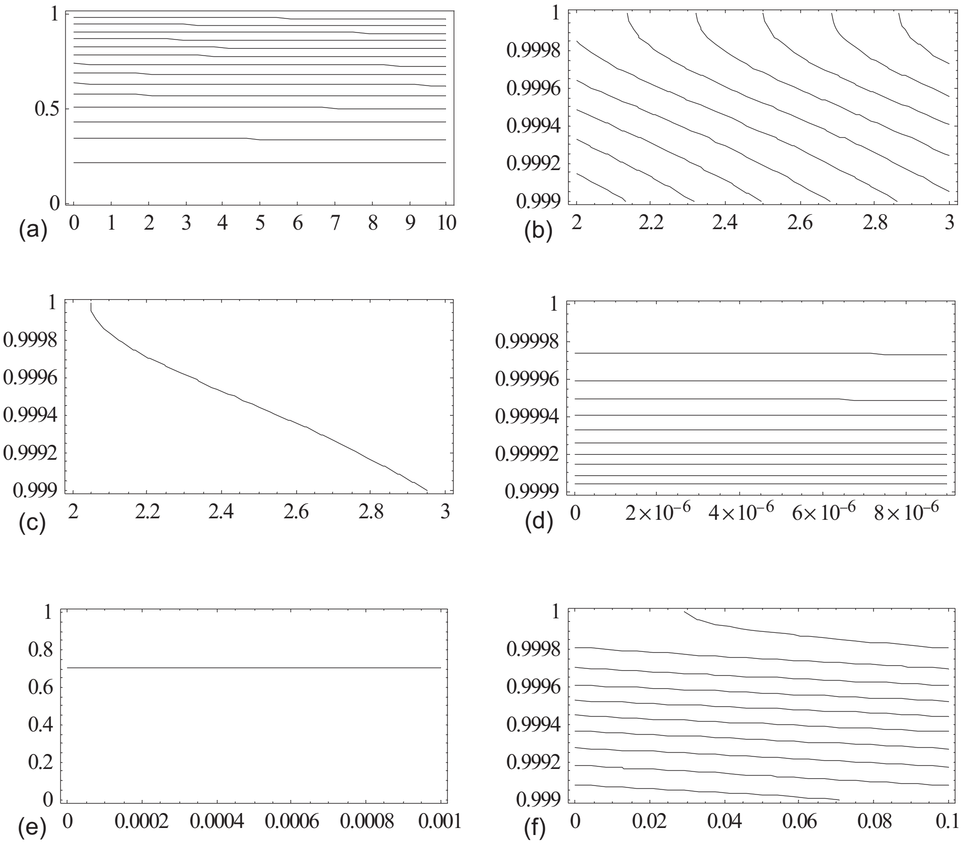

FIG. 3. Same as above except for $u_c = 1000$.

$$\beta_n \int_0^1 (2n+1)\cos^2\left[\left(n+\tfrac{1}{2}\right)\pi r^2\right] r dr = \frac{1}{\pi}\int_0^1 u_0(r)\cos\left[\left(n+\tfrac{1}{2}\right)\pi r^2\right] r dr \tag{19}$$

or

$$\beta_n = \begin{cases} \dfrac{4\int_0^1 u_0(r)\cos\left[\left(n+\frac{1}{2}\right)\pi r^2\right] r dr}{\pi(2n+1)}; & \text{general} \\ \dfrac{4(-1)^n}{\pi^2(2n+1)^2}\dfrac{U_c}{U_w} = \dfrac{4(-1)^n u_c}{\pi^2(2n+1)^2}; & u_0 = u_c = \text{const.} \end{cases} \tag{20}$$

Backward substitution into Eq. (16) enables us to extract

$$\psi = \begin{cases} \displaystyle\sum_{n=0}^{\infty} (\alpha_n z + \beta_n)\sin\left[\left(n+\tfrac{1}{2}\right)\pi r^2\right]; & \text{general} \\ \displaystyle\sum_{n=0}^{\infty} \left[\alpha_n z + \frac{4(-1)^n u_c}{\pi^2(2n+1)^2}\right]\sin\left[\left(n+\tfrac{1}{2}\right)\pi r^2\right]; & u_0 = u_c. \end{cases} \tag{21}$$

Note that many solutions may be arrived at depending on the choice of α_n that properly fulfills Eq. (17). One such case corresponds to Taylor's family of solutions for which

$$\alpha_0 = 1 \quad \text{and} \quad \alpha_n = 0; \quad \forall\, n \neq 0. \tag{22}$$

At the outset, Eq. (21) reduces to

$$\psi(r,z) = \begin{cases} z\sin\left(\tfrac{1}{2}\pi r^2\right) + \displaystyle\sum_{n=0}^{\infty} \beta_n \sin\left[\left(n+\tfrac{1}{2}\right)\pi r^2\right]; & \text{general Taylor - Culick} \\ z\sin\left(\tfrac{1}{2}\pi r^2\right) + \dfrac{4u_c}{\pi^2}\displaystyle\sum_{n=0}^{\infty} \frac{(-1)^n}{(2n+1)^2}\sin\left[\left(n+\tfrac{1}{2}\right)\pi r^2\right]; & \text{Taylor - Culick with } u_0 = u_c. \end{cases} \tag{23}$$

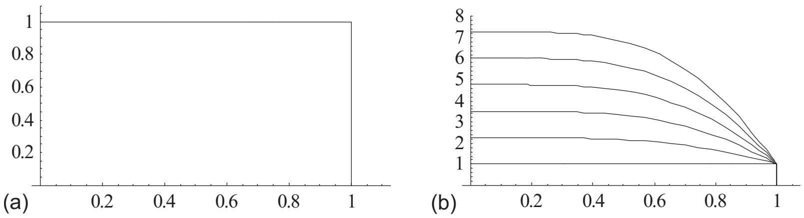

FIG. 4. Radial evolution of the streamwise velocity u_z corresponding to $u_c=1$. This value may be associated with a simulated SRM with reactive headwall. Results are shown at (a) $z=0$ and (b) six equidistant positions corresponding to $z=0$, 0.4, 0.8, 1.2, 1.6, and 2.

Note that the general Taylor-Culick profile represents a solution for uniform sidewall injection and an arbitrary headwall injection pattern $u_0(r)$ that can be captured by the general form of β_n from Eq. (20). This expression is deliberately left as an infinite series albeit collapsible into closed form when put in terms of special functions. The classical Taylor-Culick solution with inert headwall is easily recovered by setting $\beta_n=0; \forall n$, $\alpha_0=1$ and $\alpha_n=0; \forall n \neq 0$.

The character of Eq. (23) is illustrated in Fig. 2 for a uniform headwall injection rate appropriate of SRMs with reactive head end. Using $u_0=u_c=1$, a balance between sidewall and headwall injection causes the streamline originating at the corner (1,0) to bisect the flow field at an angle of $\pi/4$. By concentrating on specific areas, it may be seen that the solution conforms to the stated boundary conditions. While Fig. 2(b) illustrates the corner streamlines, Figs. 2(c) and 2(d) confirm the satisfaction of the no slip condition by reproducing the local behavior in different sectors. Similarly, Figs. 2(e) and 2(f) confirm the headwall injection boundary condition.

When the same analysis is repeated in Fig. 3 for $u_c=1000$, a stream tube motion akin to that of hybrid rocket core flow is seen to dominate. This is true everywhere except in the close vicinity of the sidewall. While Fig. 3(a) offers an overview of the stream tube motion, magnification near the sidewalls enables us to reaffirm that the fluid enters the chamber perpendicularly to the sidewall. By approaching the headwall, the presence of parallel flow in Figs. 3(e) and 3(f) lends support to the local orthogonality.

Having found ψ, the velocity and vorticity components may be recovered from Eqs. (6) and (8). One obtains $u_r(r)=-r^{-1}\sin(\pi r^2/2)$ for all cases and

$$u_z(r,z)=\begin{cases}\pi z\cos\left(\frac{1}{2}\pi r^2\right)+\pi\sum_{n=0}^{\infty}(2n+1)\beta_n\cos\left[\left(n+\frac{1}{2}\right)\pi r^2\right]; & \text{general Taylor-Culick}\\ \pi z\cos\left(\frac{1}{2}\pi r^2\right)+\frac{4u_c}{\pi}\sum_{n=0}^{\infty}\frac{(-1)^n}{(2n+1)}\cos\left[\left(n+\frac{1}{2}\right)\pi r^2\right]; & \text{Taylor-Culick with } u_0=u_c\end{cases}\tag{24}$$

$$\Omega(r,z)=\begin{cases}\pi^2 rz\sin\left(\frac{1}{2}\pi r^2\right)+\pi^2 r\sum_{n=0}^{\infty}(2n+1)^2\beta_n\sin\left[\left(n+\frac{1}{2}\right)\pi r^2\right]; & \text{general Taylor-Culick}\\ \pi^2 rz\sin\left(\frac{1}{2}\pi r^2\right); & \text{Taylor-Culick with } u_0=u_c.\end{cases}\tag{25}$$

Note that uniform headwall injection does not alter the radial velocity nor does it introduce any mean flow vorticity. Furthermore, one may confirm that $u_z(1,z)=0$ because each $\cos\left[\left(n+\frac{1}{2}\right)\pi\right]$ term vanishes along the sidewall. This behavior is illustrated in Figs. 4(a) and 4(b) at the headwall and, using $L=2$, at six equally spaced axial stations corresponding to 0, 0.4, 0.8, 1.2, 1.6, and 2. It may be interesting to note that the streamwise velocity is also collapsible into closed form by recognizing that, for uniform headwall injection,

$$\frac{4u_c}{\pi}\sum_{n=0}^{\infty}\frac{(-1)^n}{(2n+1)}\cos\left[\left(n+\frac{1}{2}\right)\pi r^2\right]=\frac{2u_c}{\pi}q(r);$$
$$q(r)=\tan^{-1}(e^{\mathbf{i}\pi r^2/2})+\tan^{-1}(e^{-\mathbf{i}\pi r^2/2}).\tag{26}$$

B. Solution by injection-driven eigenfunctions

The same analysis may be repeated by retaining only the even eigenvalues associated with an injection-driven wall contribution. This can be seen by reconsidering Eq. (14) and selecting

$$C=C_n=(4n+1)\pi;\ n\in\mathbb{Z}.\tag{27}$$

This choice enables us to skip every other multiple of $\pi/2$, thus producing a series of injection-based solutions. The third condition becomes

$$\sum_{n=-\infty}^{\infty}\alpha_n\sin\left[\left(2n+\frac{1}{2}\right)\pi\right]=1 \quad \text{or} \quad \sum_{n=-\infty}^{\infty}\alpha_n=1.\tag{28}$$

Note that we start our sum at negative infinity lest we capture half of the headwall injection velocity. As we pursue this route, the headwall requirement reduces to

$$\pi \sum_{n=-\infty}^{\infty} (4n+1)\beta_n \cos\left[\left(2n+\tfrac{1}{2}\right)\pi r^2\right] = u_0 \tag{29}$$

and so, by use of orthogonality, we reap

$$\beta_n = \begin{cases} \dfrac{4\int_0^1 u_0(r)\cos\left[\left(2n+\frac{1}{2}\right)\pi r^2\right] r dr}{\pi(4n+1)}; & \text{general} \\ \dfrac{4u_c}{\pi^2(4n+1)^2}; & u_0 = u_c. \end{cases} \tag{30}$$

The injection-based stream function becomes

$$\psi_{\text{inj}} = \begin{cases} \displaystyle\sum_{n=-\infty}^{\infty} (\alpha_n z + \beta_n)\sin\left[\left(2n+\tfrac{1}{2}\right)\pi r^2\right]; & \text{general} \\ \displaystyle\sum_{n=-\infty}^{\infty} \left[\alpha_n z + \frac{4u_c}{\pi^2(4n+1)^2}\right]\sin\left[\left(2n+\frac{1}{2}\right)\pi r^2\right]; & u_0 = u_c. \end{cases} \tag{31}$$

Note that both ψ_{inj} and ψ are equivalent representations.

C. Nonlinear residual in the vorticity transport equation

Based on Eq. (4), the residual Q of the vorticity transport equation may be calculated from

$$Q(r,z) = \|\nabla \times \mathbf{u} \times \mathbf{\Omega}\| = -\left[\frac{\partial}{\partial r}(u_r\Omega) + \frac{\partial}{\partial z}(u_z\Omega)\right]. \tag{32}$$

In terms of the stream function, we therefore have

$$Q = -\frac{\Omega}{r^2}\frac{\partial\psi}{\partial z} + \frac{1}{r}\frac{\partial\psi}{\partial z}\frac{\partial\Omega}{\partial r} - \frac{1}{r}\frac{\partial\psi}{\partial r}\frac{\partial\Omega}{\partial z}. \tag{33}$$

For each eigensolution given by Eq. (21), the vorticity transport equation vanishes upon substitution. Using $\Omega = \Omega_n = C_n^2 r\psi_n$, Eq. (33) becomes

$$\begin{aligned} Q_n &= -\frac{C_n^2\psi_n}{r}\frac{\partial\psi_n}{\partial z} + \frac{1}{r}\frac{\partial\psi_n}{\partial z}\frac{\partial}{\partial r}(C_n^2 r\psi_n) - \frac{1}{r}\frac{\partial\psi_n}{\partial r}\frac{\partial}{\partial z}(C_n^2 r\psi_n) \\ &= -\frac{C_n^2\psi_n}{r}\frac{\partial\psi_n}{\partial z} + \frac{1}{r}\frac{\partial\psi_n}{\partial z}C_n^2\psi_n + C_n^2\frac{\partial\psi_n}{\partial z}\frac{\partial\psi_n}{\partial r} \\ &\quad - C_n^2\frac{\partial\psi_n}{\partial r}\frac{\partial\psi_n}{\partial z} = 0. \end{aligned} \tag{34}$$

The summation of Eq. (34) over all eigenmodes is identically zero. However, when coupling between eigenmodes is considered, the total vorticity and stream function must be accounted for in the vorticity transport equation. Substitution into Eq. (33) requires evaluating

$$\begin{aligned} Q &= -\frac{1}{r^2}\sum_{n=0}^{m}\Omega_n\sum_{n=0}^{m}\frac{\partial\psi_n}{\partial z} + \frac{1}{r}\sum_{n=0}^{m}\frac{\partial\psi_n}{\partial z}\sum_{n=0}^{m}\frac{\partial\Omega_n}{\partial r} \\ &\quad - \frac{1}{r}\sum_{n=0}^{m}\frac{\partial\psi_n}{\partial r}\sum_{n=0}^{m}\frac{\partial\Omega_n}{\partial z}. \end{aligned} \tag{35}$$

Then, by taking into account that

$$\begin{aligned} &\psi_n(r,z) = (\alpha_n z + \beta_n)\sin\left(\tfrac{1}{2}C_n r^2\right); \quad \frac{\partial\psi_n}{\partial z}(r) = \alpha_n \sin\left(\tfrac{1}{2}C_n r^2\right) \\ &\frac{\partial\psi_n}{\partial r}(r,z) = rC_n(\alpha_n z + \beta_n)\cos\left(\tfrac{1}{2}C_n r^2\right); \quad \frac{\partial\Omega_n}{\partial z}(r) = rC_n^2\alpha_n \sin\left(\tfrac{1}{2}C_n r^2\right) \end{aligned} \tag{36}$$

and, for the Taylor-Culick class of solutions, $\alpha_0 = 1$ and $\alpha_n = 0$ ($\forall n \neq 0$), one is left with

$$\frac{\partial\psi_n}{\partial z} = \begin{cases} \alpha_0 \sin\left(\tfrac{1}{2}C_0 r^2\right) & n = 0 \\ 0 & \forall n \neq 0 \end{cases}$$

$$\frac{\partial\Omega_n}{\partial z} = \begin{cases} C_0^2 r\alpha_0 \sin\left(\tfrac{1}{2}C_0 r^2\right) = C_0^2 r\dfrac{\partial\psi_0}{\partial z} & n = 0 \\ 0 & \forall n \neq 0 \end{cases} \tag{37}$$

where the axial derivatives are solely due to the zeroth eigenmode. This reduces Eq. (35) into

$$Q = \frac{\partial\psi_0}{\partial z}\left(-\frac{1}{r^2}\sum_{n=0}^{m}\Omega_n + \frac{1}{r}\sum_{n=0}^{m}\frac{\partial\Omega_n}{\partial r} - C_0^2\sum_{n=0}^{m}\frac{\partial\psi_n}{\partial r}\right). \tag{38}$$

We may skip the $n=0$ case for which the residual vanishes. Finally, noting that

$$\frac{\partial\Omega_n}{\partial r} = C_n^2\psi_n + C_n^2 r\frac{\partial\psi_n}{\partial r} \tag{39}$$

we retrieve

$$Q(r) = \frac{\partial\psi_0}{\partial z}\sum_{n=0}^{m}(C_n^2 - C_0^2)\frac{\partial\psi_n}{\partial r}. \tag{40}$$

Equation (40) represents the net residual of the vorticity transport equation due to nonlinear coupling; it is not necessarily zero except for inert or sinusoidal headwall injection

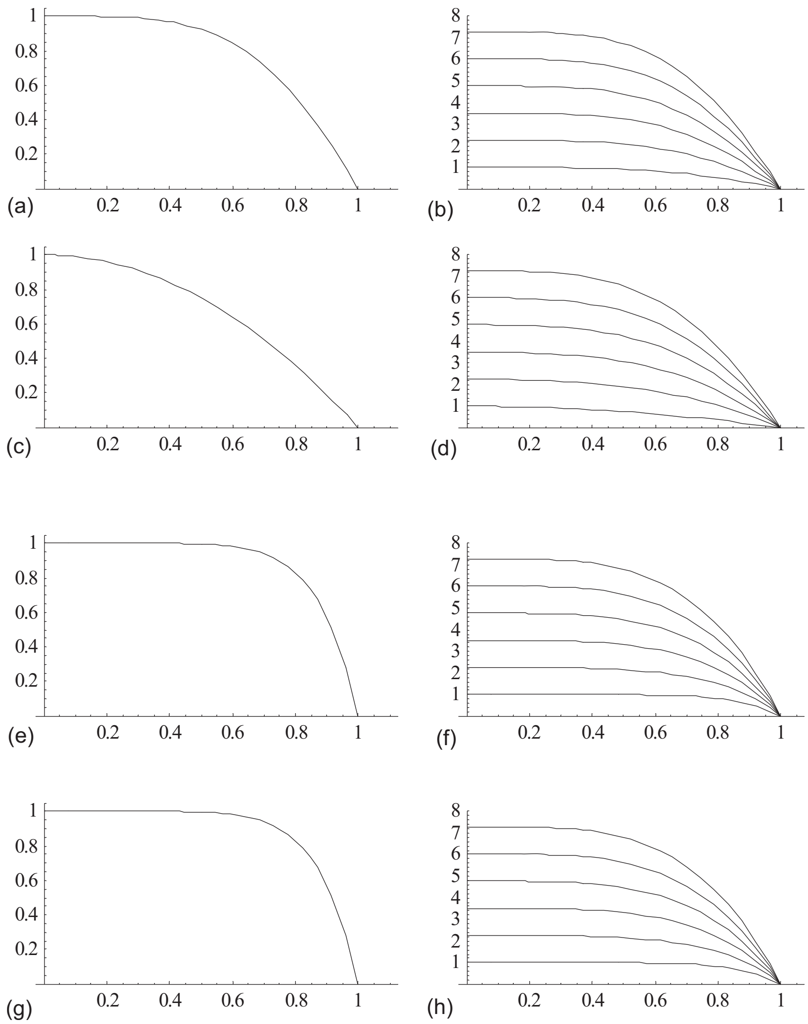

FIG. 5. Radial evolution of the streamwise velocity for $u_c=1$ and several headwall inlet profiles associated with (a)–(b) Berman's half-cosine, (c)–(d) Poiseuille, $1-r^2$, (e)–(f) $1-r^8$, and (g)–(h) $(1-r)^{1/7}$. As in Fig. 4, results are shown at the headwall (left) and six equidistant positions corresponding to $z=0$, 0.4, 0.8, 1.2, 1.6, and 2 (right).

profiles. Based on the general Taylor-Culick solution of Eq. (23), one recovers

$$Q(r) = r\sin\left(\tfrac{1}{2}\pi r^2\right)\sum_{n=0}^{m}(C_n^2 - C_0^2)C_n\beta_n\cos\left(\tfrac{1}{2}C_n r^2\right)$$
$$\sim \tfrac{1}{2}\pi r^3\sum_{n=0}^{m}(C_n^2 - C_0^2)C_n\beta_n + O(r^5)$$
$$\sim 2\pi r^3\sum_{n=0}^{m}\left[(2n+1)^2\pi^2 - \pi^2\right]\int_0^1 u_0(r)$$
$$\times\cos\left[\left(n+\tfrac{1}{2}\right)\pi r^2\right]r\mathrm{d}r + O(r^5). \tag{41}$$

Clearly, solutions with modes for which $C_n^2 - C_0^2 \neq 0$ entail a residual and become, at the outset, nonexact. However, being independent of z, the residual becomes relatively smaller as we move away from the headwall. Furthermore, the solution becomes more accurate near the sidewall boundary and along the centerline where the residual vanishes identically. The diminution in the streamwise direction makes the approximation appropriate for long SRMs. The behavior is also consistent with the Taylor-Culick model which is known for its subtle discontinuity at $z=0$. In all cases, the core flow approximations become increasingly more accurate away from the headwall, a condition that is compatible with the parallel flow assumption used in many stability studies of SRM flow fields.[20–22]

D. Pressure analysis

The steady momentum equation may be readily solved for the pressure distribution. By ignoring viscous diffusion, one may start with $\mathbf{u}\cdot\nabla\mathbf{u} = -\nabla p$ and integrate in two spatial directions to retrieve, at length,

$$p = p_0 - \tfrac{1}{2}\mathbf{u}\cdot\mathbf{u} - \int u_r \frac{\partial u_z}{\partial r} dz \tag{42}$$

where $p_0 = p(0,0)$ represents the headwall pressure. Immediate integration and substitution based on Eq. (24) and uniform headwall injection lead to

$$p = p_0 - \tfrac{1}{2}\pi^2 z^2 - \tfrac{1}{2}r^{-2}\sin^2\left(\tfrac{1}{2}\pi r^2\right) + \tfrac{1}{2}u_c^2 - 2\pi^{-2}u_c q(r)$$
$$\times\left[u_c q(r) + \pi^2 z\cos\left(\tfrac{1}{2}\pi r^2\right)\right]. \tag{43}$$

At this juncture, one may use $q(r) = \tfrac{1}{2}\pi[1-\delta_k(1-r)]$ and write

$$p = p_0 - \tfrac{1}{2}\pi^2 z^2 - \tfrac{1}{2}r^{-2}\sin^2\left(\tfrac{1}{2}\pi r^2\right) + \tfrac{1}{2}u_c^2\delta_k(1-r)$$
$$- \pi u_c z\cos\left(\tfrac{1}{2}\pi r^2\right)[1-\delta_k(1-r)] \tag{44}$$

where δ_k is the Kronecker delta. At the centerline, we re-

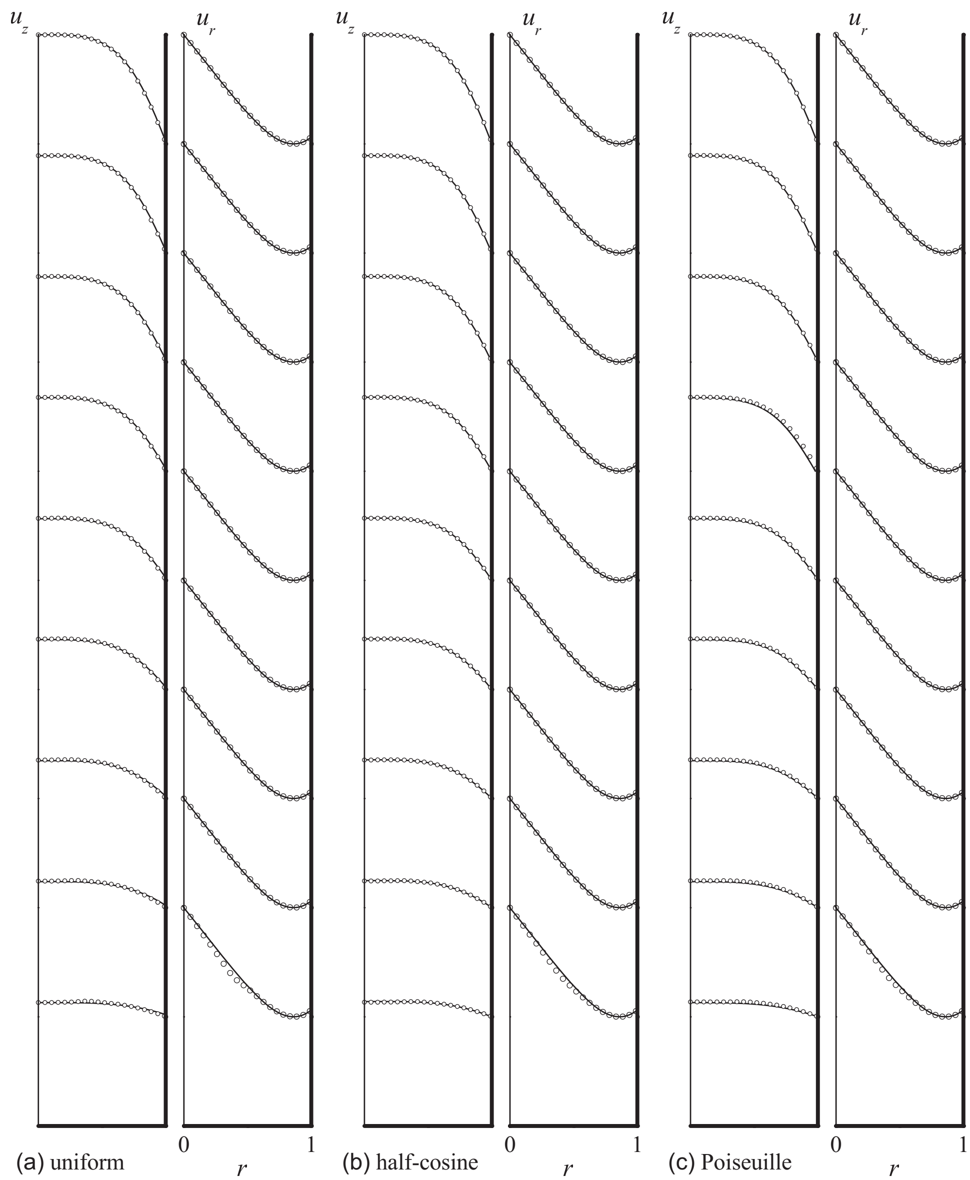

FIG. 6. Comparison between inviscid analytical and numerical simulations for (a) uniform, (b) half-cosine, and (c) Poiseuille injection profiles in a cylindrical chamber using $U_w=10$ m/s and $u_c=1,\pi/2,2$, respectively. Hollow circles denote computational results. Axial positions correspond to $z/L=0.1,0.2,0.3,\ldots,0.9$.

cover $p(0,z)=p_0-\frac{1}{2}\pi^2z^2-\pi u_c z$. To put this in Culick's traditional form, we first write the dimensional pressure, $\bar{p}=\bar{p}_0-\frac{1}{2}\rho U_w^2\pi z(\pi z+2u_c)$, and then renormalize by $\bar{p}_0=\rho a_0^2/\gamma$ (based on the speed of sound a_0 and ratio of specific heats γ). We get

$$\begin{aligned} p^* = \bar{p}/\bar{p}_0 &= 1-\tfrac{1}{2}\gamma M_w^2\Big\{\pi^2z^2+r^{-2}\sin^2\!\left(\tfrac{1}{2}\pi r^2\right)-u_c^2 \\ &\quad +4\pi^{-2}u_c q(r)\left[u_c q(r)+\pi^2 z\cos\!\left(\tfrac{1}{2}\pi r^2\right)\right]\Big\} \\ &= 1-\tfrac{1}{2}\gamma M_w^2\Big\{\pi^2z^2+r^{-2}\sin^2\!\left(\tfrac{1}{2}\pi r^2\right) \\ &\quad -u_c^2\delta_k(1-r)+2\pi u_c z\cos\!\left(\tfrac{1}{2}\pi r^2\right) \\ &\quad \times[1-\delta_k(1-r)]\Big\} \end{aligned} \tag{45}$$

with $p^*(0,z)=1-\frac{1}{2}\gamma M_w^2\pi z(\pi z+2u_c)$. This matches Culick's result for the impervious headwall ($u_c=0$).

E. Variable headwall injection profile

The analysis may be illustrated using a variable headwall injection profile. To be specific, one may use

$$u_0(r)=\begin{cases} u_c\cos\!\left(\tfrac{1}{2}\pi r^2\right) & \text{(a)} \\ u_c(1-r^m) & \text{(b)} \\ u_c(1-r)^{1/m} & \text{(c).} \end{cases} \tag{46}$$

These are prescribed by classic profiles used by Berman (i.e., the half-cosine),[23] Poiseuille, and others. For uniform headwall injection, it is evident that $u_0=u_c=1$ corresponds to a simulated solid propellant grain that is burning evenly along its surfaces. However, when the headwall injection profile is altered according to Eq. (46), the centerline speed needed to

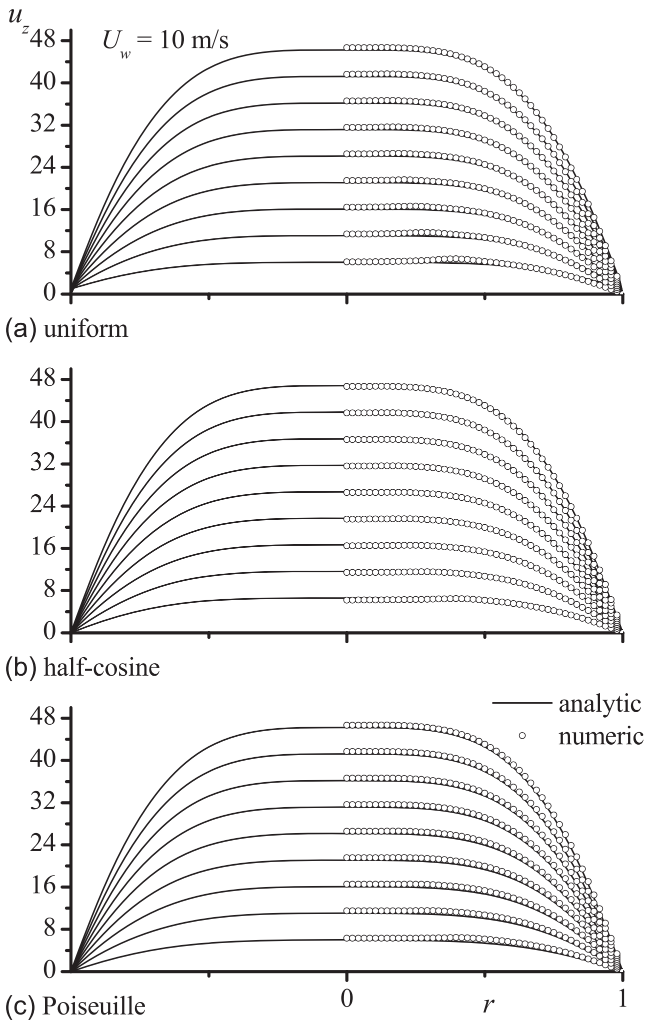

FIG. 7. Same as above except for the axial velocities being enlarged for better comparison.

produce the same flux at $z=0$ may be calculated from a simple mass balance, namely,

$$2\int_0^1 u_0(r) r dr = 1 \quad \text{or} \quad u_c = \begin{cases} \frac{1}{2}\pi & \text{(a)} \\ (m+2)/m & \text{(b)} \\ (m+1)\left(m+\frac{1}{2}\right)/m^2 & \text{(c)}. \end{cases} \tag{47}$$

In all cases, one may obtain the Taylor-Culick solution from Eq. (23). For Berman's half-cosine, we use Eq. (20) to get $\beta_0 = u_c/\pi$ and $\beta_n = 0, n \neq 0$. Equation (24) becomes

$$\begin{aligned} u_z &= \pi z \cos\left(\tfrac{1}{2}\pi r^2\right) + u_c \cos\left(\tfrac{1}{2}\pi r^2\right) \\ &= \pi(z + u_h)\cos\left(\tfrac{1}{2}\pi r^2\right); \quad u_h \equiv u_c/\pi. \end{aligned} \tag{48}$$

This step restores the solution applied by Majdalani and Vyas[19] for modeling hybrid rocket core flows.

For the Poiseuille profile, one may use $u_0(r) = u_c(1-r^2)$ to obtain

$$\beta_n = 8u_c/\lambda_n^3; \quad \lambda_n \equiv \pi + 2n\pi. \tag{49}$$

Both Berman's and Poiseuille's headwall injection velocities are illustrated in Fig. 5 using the same representative parameters of Fig. 4 and fixed $u_c = 1$. As evidenced by the right-hand side graphs, the effect of varying the headwall injection profile becomes negligible as the chamber length is increased. However, it remains important near the headwall and, particularly, in short chambers such as those entailed in upper stage SRMs and T-burners. As for the turbulent profiles corresponding to Eq. (46), three commonly examined cases may be connected with $m = 6, 8, 10$. These lead to

$$\frac{\lambda_n^{2+m/2}\beta_n}{u_c} = \begin{cases} 96[(-1)^n\lambda_n - 2] & m=6 \\ 192(-1)^n(\lambda_n^2 - 8) & m=8 \\ 320[(-1)^n\lambda_n(\lambda_n^2 - 24) + 48] & m=10 \end{cases} \quad \text{where } u_c = \begin{cases} 4/3 & m=6 \\ 5/4 & m=8 \\ 6/5 & m=10. \end{cases} \tag{50}$$

Finally, for the turbulent model associated with Eq. (46), one may obtain a recursive relation in terms of the generalized hypergeometric function ${}_pF_q(a;b;z) = {}_pF_q(\{a_1,\ldots,a_p\};\{b_1,\ldots,b_q\};z)$; for our specific cases, we find the arguments to be $p=3$ and $q=4$ such that

$$\beta_n = \frac{4m^2 u_c}{(1+m)(1+2m)\lambda_n} {}_3F_4\left(\left\{\tfrac{3}{4}, 1, \tfrac{5}{4}\right\},\right.$$

$$\left.\left\{\tfrac{3}{4} + \tfrac{1}{4m}, 1 + \tfrac{1}{4m}, \tfrac{5}{4} + \tfrac{1}{4m}, \tfrac{3}{2} + \tfrac{1}{4m}\right\}, -\tfrac{1}{16}\lambda_n^2\right); \tag{51}$$

$$u_c = \begin{cases} 91/72 & m=6 \\ 60/49 & m=7 \\ 153/128 & m=8. \end{cases}$$

The commonly employed (middle) values in Eqs. (50) and (51) are illustrated in Figs. 5(e)–5(h) using a fixed $u_c = 1$.

IV. NUMERICAL VERIFICATION

So far we have described an approximate Euler solution for the Taylor-Culick flow with variable headwall injection. By way of confirmation, we now present an inviscid numerical solution for the mean flow field using three illustrative headwall injection profiles. Our simulations are carried out using a pressure-based, finite volume, unstructured, two-dimensional code. The targeted flow is that corresponding to a rocket motor with an average sidewall Mach number of 0.03 and purely inviscid conditions. The large sidewall Mach number is deliberately chosen to draw attention to the flow behavior near the boundaries and its ability to observe the wall-normal injection requirement. The aspect ratio of the domain is set at $L=16$. The actual length and radius are taken at $1.6\ \text{m}\times 0.1\ \text{m}$ and the wall injection velocity is taken at $10\ \text{m/s}$ for the simulated SRM. The boundary conditions at the sidewall are specified as velocity inlets to closely mimic the mathematical model where injection is imposed uniformly along the grain surface. The headwall is also specified as an inlet. On the right-hand side of the domain a pressure outlet boundary condition is prescribed. Although an outflow boundary condition can also be imposed at the downstream section, it is discounted here to avoid the possible case of partially developed flow. The difference between an outflow and a pressure outlet boundary condition is that, in the latter case, the exit pressure is fixed at the boundary. The domain is meshed into 589 824 equally spaced control volumes (3072×192). While the first order upwind is called upon for spatial discretization, the SIMPLE algorithm is used to handle pressure and velocity.

Results for the inviscid simulations are shown in Figs. 6 and 7. These are carried out for $u_c=1,\pi/2,2$ and show the streamwise evolution of the axial and transverse velocities at $z/L=0.1,0.2,0.3,\ldots,0.9$. For the sake of comparison, the working fluid is taken to be ambient air. It may be seen that the agreement with the computations is excellent. These limited numerical experiments reaffirm the viability of the analytical approximations described above.

V. CONCLUSIONS

In this study we revisit the incompressible Taylor-Culick flow problem with arbitrary headwall injection. Two solutions are obtained that satisfy the principal surface requirements including the velocity adherence condition on the wall. The two formulations are found to yield identical results. Their behavior is illustrated for the cases of small and large headwall injection pertaining, for example, to SRM and hybrid rocket models, respectively. The analysis encompasses not only uniform but variable inlet velocities. We find the effect of varying the headwall injection profile to be small in sufficiently long chambers. However, it plays a key role in short chambers and T-burners where the foregoing formulations may be applied. In hybrid rockets, our models are seen to capture the stream tube motion quite effectively. The expressions presented here increase our repertoire of engineering approximations for the modeling of injection-driven porous tubes. In future work, we hope to consider other geometric shapes that are of interest to the propulsion community.

ACKNOWLEDGMENTS

This work is sponsored by the National Science Foundation through Grant No. CMS-0353518. The principal author acknowledges valuable discussions with Dr. Grégoire Casalis, Professor and Director of the Doctoral School of Aeronautics and Astronautics, SUPAERO, and Research Director, Department of Aerodynamics and Energetics, ONERA, Toulouse, France.

[1] F. E. C. Culick, "Rotational axisymmetric mean flow and damping of acoustic waves in a solid propellant rocket," AIAA J. **4**, 1462 (1966).
[2] G. I. Taylor, "Fluid flow in regions bounded by porous surfaces," Proc. R. Soc. London, Ser. A **234**, 456 (1956).
[3] R. Dunlap, P. G. Willoughby, and R. W. Hermsen, "Flow field in the combustion chamber of a solid propellant rocket motor," AIAA J. **12**, 1440 (1974).
[4] J. D. Baum, J. N. Levine, and R. L. Lovine, "Pulsed instabilities in rocket motors: A comparison between predictions and experiments," AIAA J. **4**, 308 (1988).
[5] J. S. Sabnis, H. J. Gibeling, and H. McDonald, "Navier-Stokes analysis of solid propellant rocket motor internal flows," AIAA J. **5**, 657 (1989).
[6] K. Yamada, M. Goto, and N. Ishikawa, "Simulative study of the erosive burning of solid rocket motors," AIAA J. **14**, 1170 (1976).
[7] R. Dunlap, A. M. Blackner, R. C. Waugh, R. S. Brown, and P. G. Willoughby, "Internal flow field studies in a simulated cylindrical port rocket chamber," AIAA J. **6**, 690 (1990).
[8] C. D. Clayton, "Flowfields in solid rocket motors with tapered bores," AIAA Paper 96-2643, Lake Buena Vista, Fl, 1996.
[9] S. Balachandar, J. D. Buckmaster, and M. Short, "The generation of axial vorticity in solid-propellant rocket-motor flows," J. Fluid Mech. **429**, 283 (2001).
[10] J. Majdalani and T. S. Roh, "The oscillatory channel flow with large wall injection," Proc. R. Soc. London, Ser. A **456**, 1625 (2000).
[11] J. Majdalani and G. A. Flandro, "The oscillatory pipe flow with arbitrary wall injection," Proc. R. Soc. London, Ser. A **458**, 1621 (2002).
[12] P. Kuentzmann, *Combustion Instabilities* (AGARDograph, Princeton University, Princeton, 1991).
[13] J. C. Traineau, P. Hervat, and P. Kuentzmann, "Cold-flow simulation of a two-dimensional nozzleless solid-rocket motor," AIAA Paper 86-1447, Huntsville, AL, 1986.
[14] S. Apte and V. Yang, "Effect of acoustic oscillation on flow development in a simulated nozzleless rocket motor," in *Solid Propellant Chemistry, Combustion, and Motor Interior Ballistics*, edited by V. Yang, T. B. Brill, and W.-Z. Ren (AIAA, Washington, D.C., 2000), Vol. 185, pp. 791–822.
[15] J. Griffond, G. Casalis, and J.-P. Pineau, "Spatial instability of flow in a semiinfinite cylinder with fluid injection through its porous walls," Eur. J. Mech. B/Fluids **19**, 69 (2000).
[16] J. Griffond and G. Casalis, "On the nonparallel stability of the injection induced two-dimensional Taylor flow," Phys. Fluids **13**, 1635 (2001).
[17] T. Féraille and G. Casalis, "Channel flow induced by wall injection of fluid and particles," Phys. Fluids **15**, 348 (2003).
[18] J. Majdalani, A. B. Vyas, and G. A. Flandro, "Higher mean-flow approximation for a solid rocket motor with radially regressing walls," AIAA J. **40**, 1780 (2002).
[19] J. Majdalani and A. B. Vyas, "Inviscid models of the classic hybrid rocket," AIAA Paper 2004-3474, Fort Lauderdale, FL, 2004.
[20] J. Griffond and G. Casalis, "On the dependence on the formulation of some nonparallel stability approaches applied to the Taylor flow," Phys. Fluids **12**, 466 (2000).
[21] Y. Fabignon, J. Dupays, G. Avalon, F. Vuillot, N. Lupoglazoff, G. Casalis, and M. Prévost, "Instabilities and pressure oscillations in solid rocket motors," Aerosp. Sci. Technol. **7**, 191 (2003).
[22] F. Chedevergne, G. Casalis, and T. Féraille, "Biglobal linear stability analysis of the flow induced by wall injection," Phys. Fluids **18**, 014103–14 (2006).
[23] A. S. Berman, "Laminar flow in channels with porous walls," J. Appl. Phys. **24**, 1232 (1953).